Chinese Chemical Letters 32 (2021) 511–515

Contents lists available at ScienceDirect

Chinese Chemical Letters

journal homepage: www.elsevier.com/locate/cclet

Communication

Ruthenium nanoclusters anchored on cobalt phosphide hollow microspheres by green phosphating process for full water splitting in acidic electrolyte

Yunqie Deng[a], Linjing Yang[a,b], Yakun Wang[a], Lili Zeng[a], Jiayuan Yu[a], Bo Chen[c], Xiaoli Zhang[d,**], Weijia Zhou[a,b,*]

[a] *Guangzhou Key Laboratory for Surface Chemistry of Energy Materials, New Energy Research Institute, School of Environment and Energy, South China University of Technology, Guangzhou Higher Education Mega Center, Guangzhou 510006, China*
[b] *Shandong Collaborative Innovation Center of Technology and Equipements for Biological Diagnosis and Therapy, Institute for Advanced Interdisciplinary Research (iAIR), University of Jinan, Ji'nan 250022, China*
[c] *Center for Programmable Materials, School of Materials Science and Engineering, Nanyang Technological University, Singapore 639798, Singapore*
[d] *School of Materials Science and Engineering, Zhengzhou University, Zhengzhou 450001, China*

ARTICLE INFO

Article history:
Received 11 March 2020
Received in revised form 28 March 2020
Accepted 30 March 2020
Available online 15 April 2020

Keywords:
Green phosphating
Cobalt phosphide
Ruthenium nanocluster
Hydrogen evolution reaction
Water splitting

ABSTRACT

Transition metal phosphide (TMP) based electrocatalysts possessing special crystal and electronic structures attract broad attention in the field of electrocatalysis. Immense effort is made to optimize TMP catalysts aiming to satisfy the electrochemical catalysis performance. In this work, an environmentally friendly *in situ* green phosphating strategy and spatial limiting effect of the RuCo precursor is employed to fabricate the ruthenium nanoclusters anchored on cobalt phosphide hollow microspheres (Ru NCs/Co_2P HMs). The obtained Ru NCs/Co_2P HMs electrocatalysts exhibit high hydrogen evolution reaction (HER) activity at wide pH ranges, which require an overpotential of 77 mV to achieve the current density of 10 mA/cm^2 in 0.5 mol/L H_2SO_4 and 118 mV in 1.0 mol/L KOH. Besides, the multifunctional Ru NCs/Co_2P HMs exhibit good oxygen evolution reaction (OER) activity with an overpotential of 197 mV to reach the current density of 10 mA/cm^2 in 0.5 mol/L H_2SO_4, which is below that of the commercial RuO_2 electrocatalyst (248 mV). A two-electrode electrolyzer is assembled as well, in acid electrolyte, it achieves a current density of 10 mA/cm^2 at a voltage of 1.53 V, which is superior to that of the benchmark of precious metal-based electrolyzer (1.58 V).

Hydrogen as a sustainable, clean and efficient energy resource has been considered as one of the most promising future energy [1–6]. The sanitary production of hydrogen by electrolysis of water is regarded as an ideal technology without any detrimental by-products and pollutants. Therefore, the high-efficiency and steady electrocatalysts are essential to water electrolysis. Accordingly, evolving highly active electrocatalysts is fundamental to meet the hydrogen production. Recently, cobalt phosphide and its derivatives [7–9] who belongs to a class of transition metal phosphides (TMPs) exhibit excellent hydrogen evolution reaction (HER) performance *via* a hydrogenase-like catalytic mechanism [10–13]. Unfortunately, traditional synthetic strategies of metal phosphide need extrinsic phosphorus sources, for example, red phosphorus and sodium hypophosphite, which leading to dangerous phosphating process and toxic phosphine [14–16].

Herein, we presented an *in situ* green phosphating strategy without any extrinsic phosphorus sources for ruthenium nanoclusters anchored on cobalt phosphide hollow microspheres (Ru NCs/Co_2P HMs), which exhibited remarkable tolerance of wide-pH and multifunctional electrocatalyst for HER and oxygen evolution reaction (OER). The phosphorus source was derived from its own phosphate group of cobaltous phosphate, which was reduced by hydrogen atmosphere to break the P—O bonds.

The synthesis process for the Ru NCs/Co_2P HMs was shown in Scheme 1. Firstly, RuCo precursor was synthesized using a hydrothermal approach, of which the X-ray diffraction (XRD)

---

[*] Corresponding author at: Guangzhou Key Laboratory for Surface Chemistry of Energy Materials, New Energy Research Institute, School of Environment and Energy, South China University of Technology, Guangzhou Higher Education Mega Center, Guangzhou 510006, China.
[**] Corresponding author.
E-mail addresses: xiaolizhang.z@gmail.com (X. Zhang), eszhouwj@scut.edu.cn (W. Zhou).

https://doi.org/10.1016/j.cclet.2020.03.076
1001-8417/

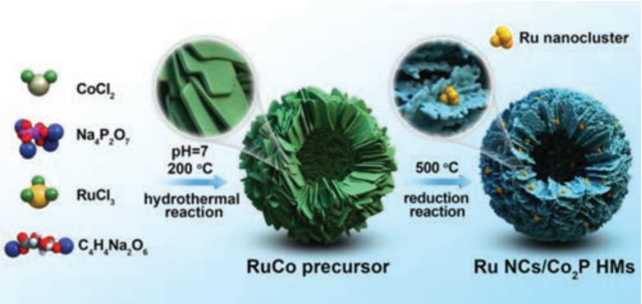

Scheme 1. Schematic illustration of the synthetic procedure for Ru NCs/Co_2P HMs.

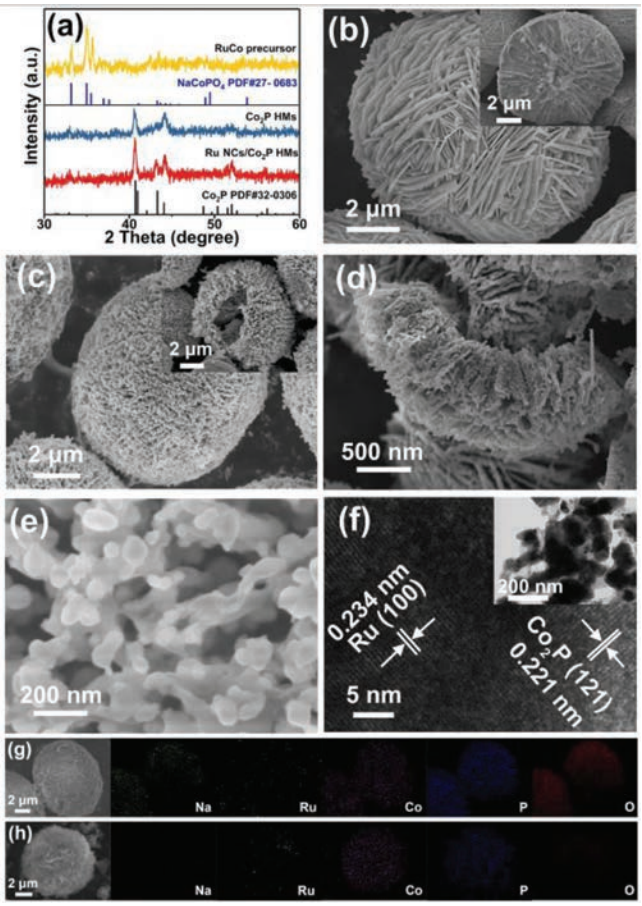

Fig. 1. (a) XRD pattern of RuCo precursor, Ru NCs/Co_2P HMs and Co_2P HMs. Typical SEM images of (b) RuCo precursor and (c–e) Ru NCs/Co_2P HMs. (f) HR-TEM image of the Ru NCs/Co_2P HMs. EDX mapping of the (g) RuCo precursor and (h) Ru NCs/Co_2P HMs.

characteristic diffraction peaks at 33.1°, 34.9° and 35.5° indexed to (211), (031) and (012) of the $NaCoPO_4$ (JCPDS card No. 27-0683), as shown in Fig. 1a. According to scanning electron microscope (SEM) images in Fig. 1b, the microspheres of RuCo precursor was of diameter of 7–8 μm and constructed of nanosheets with thickness of 20–50 nm. The Ru nanoclusters anchored on cobalt phosphide hollow microspheres (Ru NCs/Co_2P HMs) were obtained by reduction reaction under a H_2 atmosphere. The diffraction peaks at 40.7°, 43.2°, 44.1°, 51.5°, 52.0° and 56.1° can be indexed to (121), (211), (130), (131), (002) and (320) of the Co_2P (JCPDS card No. 32-0306), suggesting the successful formation of Co_2P from the RuCo precursor. No clear diffraction peaks for Ru or Ru compounds were observed in the XRD patterns of RuCo precursor and Ru NCs/Co_2P HMs. This can be mainly attributed to the small size and low loading ratio of Ru. In Figs. 1c and d, the hollow structure of the Ru NCs/Co_2P HMs owing to an inside-out Ostwald ripening process during the long-time hydrothermal reaction process where the small crystallites in the core region of the microspheres are selectively dissolved [17,18]. However, Ru NCs/Co_2P HMs became porous and rough, leading to larger specific surface area, which was verified by Nitrogen adsorption/desorption isotherm and pore-size distribution plot, as shown in Fig. S1 (Supporting information). The nanosheets were composed of nanoparticles with sizes of 50 – 200 nm as estimated by SEM observation in Fig. 1e. Consider the previous XRD results, these particles were supposed to be Co_2P nanoparticles. Consistent with the XRD results, no obvious Ru nanoparticles were clearly distinguished by SEM in Fig. 1e and transmission electron microscope (TEM) in inset of Fig. 1f. However, the high-resolution TEM (HR-TEM) image in Fig. 1f demonstrated the high contrast of a region with two kinds of lattices with interplanar spacings of 0.234 and 0.221 nm coincided with the (100) planes of Ru and (121) planes of Co_2P, respectively, confirmed the successful synthesis of Ru nanoclusters on the surface of Co_2P nanoparticle. Further, the energy dispersive X-ray spectroscopy (EDX) element mapping in Figs. 1g and h confirmed the existence of Ru, P, Co in both RuCo precursor and Ru NCs/Co_2P HMs, which were evenly distributed throughout the microsphere. The O and Na elements in RuCo precursor were successfully removed by H_2 reduction and deionized water washing, respectively. It was worth noting that the synthesis process of Ru NCs/Co_2P HMs was an environmentally friendly technology, which only produced vapour and no toxic tail gas of phosphine when compared to the conventional synthesis approaches. The synthesis parameters were systematically optimized to study the reaction mechanism of Ru NCs/Co_2P HMs in Figs. S2–S4 (Supporting information). Finally, the synthesis parameters of Ru NCs/Co_2P HMs were optimized to be the molar ratio of Ru:Co = 1:10, pH value of 7 for hydrothermal reaction and reduction temperature of 500 °C.

In order to confirm the electron transfer between Ru and Co_2P in Ru NCs/Co_2P HMs *via in situ* one-step synthesis, the Ru nanoparticles loaded onto Co_2P HMs (Ru NPs/Co_2P HMs) were synthesized by two-step process (Fig. S5 in Supporting information). The chemical compositions and binding energies of Ru NCs/Co_2P HMs, Ru NPs/Co_2P HMs and Co_2P HMs were investigated by X-ray photoelectron spectroscopy (XPS) as shown in Fig. 2. From the survey scan of the products (Fig. 2a), the concomitant of Co, P, O elements were detected in all electrodes and the signals of Ru element existed in the Ru NCs/Co_2P HMs and Ru NPs/Co_2P HMs. The signals of C and O were connected with the equipment standard peak and surface adsorption when exposed to air, respectively. As the Ru 3d peak overlaps with the C 1s peak [19], the Ru 3p spectrums were analyzed in Fig. 2b. The peaks of Ru 3p indicated that metallic state Ru (Ru°) existed in the Ru NCs/Co_2P HMs and Ru NPs/Co_2P HMs due to the strong reducing capacity of H_2 during high-temperature calcination. Obviously, a negative shift of the Ru 3p peaks (459 eV and 481.2 eV) were observed for the Ru NCs/Co_2P HMs relative to those of Ru NPs/Co_2P HMs (460.2 eV and 483.1 eV). The negative shift indicated easier electron transfer from Co_2P to Ru in Ru NCs/Co_2P HMs. That was further confirmed by the high-resolution XPS spectra of Co 2p and P 2p in Figs. 2c and d. It was seen that the peaks of Co 2p and P 2p for Ru NCs/Co_2P HMs and Ru NPs/Co_2P HMs shifted towards higher binding energy values relative to those of Co_2P HMs. The peaks of Ru NCs/Co_2P HMs shifted more intensively compared to Ru NPs/Co_2P HMs, manifested more electron transfer between Ru clusters and Co_2P HMs, which was verified by previous research [20–22].

The chemical environment of Ru was confirmed by X-ray absorption near-edge structure (XANES) spectra of Ru K-edge. As

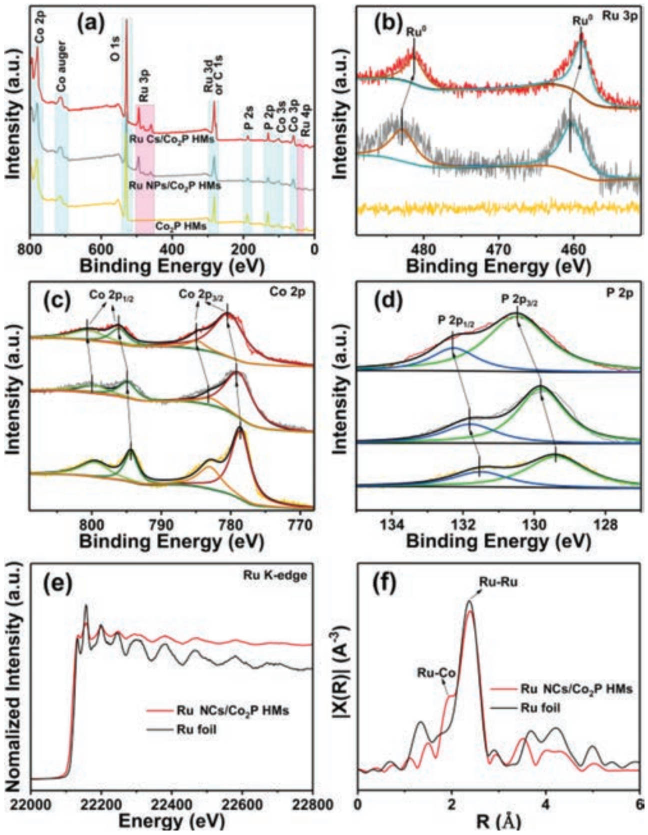

Fig. 2. (a) XPS survey spectra of Ru NCs/Co_2P HMs, Ru NPs/Co_2P HMs and Co_2P. High-resolution XPS spectrums of (b) Ru 3p, (c) Co 2p and (d) P 2p for Ru NCs/Co_2P HMs (upper panel), Ru NPs/Co_2P HMs (middle panel) and Co_2P HMs (under panel), respectively. (e) XANES spectra at Ru K-edge of Ru foil and Ru NCs/Co_2P HMs. (f) Fourier transforms of the EXFAS spectra of Ru foil and Ru NCs/Co_2P HMs.

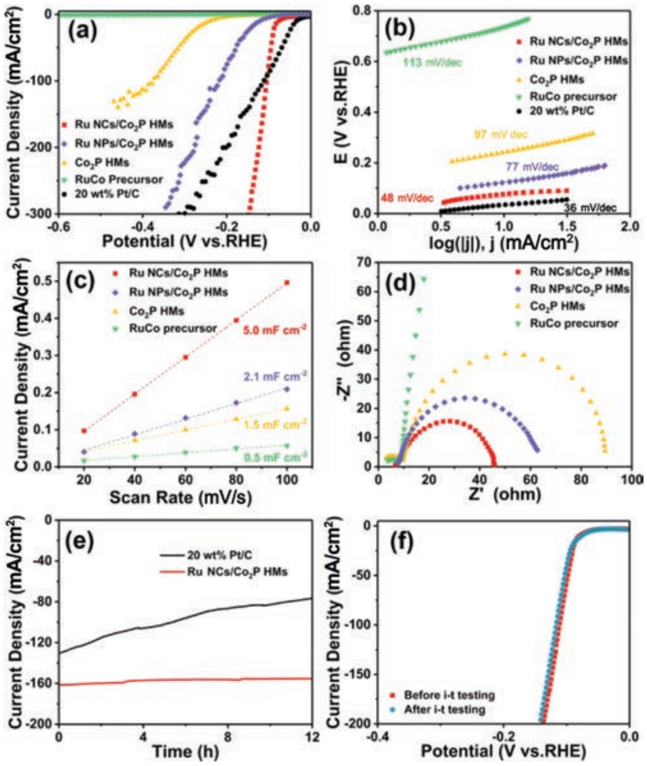

Fig. 3. (a) Polarization curves, (b) corresponding Tafel plots, (c) electrochemical area and (d) Nyquist plots at an overpotential of 200 mV of Ru NCs/Co_2P HMs, Ru NPs/Co_2P HMs, Co_2P HMs, RuCo precursor and 20 wt% Pt/C for the HER in 0.5 mol/L H_2SO_4. (e) Chronoamperometric responses for the Ru NCs/Co_2P HMs and 20 wt% Pt/C at an overpotential of 120 mV and 200 mV, respectively. (f) The polarization curves of Ru NCs/Co_2P HMs before and after *i-t* testing.

shown in Fig. 2e, the energy of absorption edge of Ru NCs/Co_2P HMs was lower than metallic Ru, indicating that the Ru bonds with Co, and Ru atom was negatively charged and Co atom was positively charged by Ru [23]. Fig. 2f showed the comparison of Fourier transform of extended X-ray absorption fine structure (EXFAS) at Ru K-edge of Ru NCs/Co_2P HMs and Ru foil. The Ru-Ru bond was main peak, which can be observed in both Ru NCs/Co_2P HMs and Ru foil. A new prominent peak appeared in Ru NCs/Co_2P HMs, which corresponding to the Ru-Co bond [24]. Combining the above data with XRD pattern (Fig. 1a) and HR-TEM image (Fig. 1f), Ru in Ru NCs/Co_2P HMs existed maybe in the form of Ru nanoclusters, which tightly bound to the surface of cobalt phosphide.

HER performance of as-synthesized electrocatalysts, including RuCo precursor, Co_2P HMs, Ru NCs/Co_2P HMs, Ru NPs/Co_2P HMs and 20 wt% Pt/C were evaluated in 0.5 mol/L H_2SO_4. As shown in Fig. 3a, RuCo precursor was inert for HER, implying the Ru ion and the phosphate were not the active sites for HER. The Ru NCs/Co_2P HMs exhibited excellent HER activity with an overpotential of 77 mV at the current density of 10 mA/cm^2 which was markedly better than those of the Co_2P HMs (241 mV@10 mA/cm^2) and Ru NPs/Co_2P HMs (122 mV@10 mA/cm^2) and closed to that of the commercial 20 wt% Pt/C (34 mV@10 mA/cm^2). The HER activity of Ru NCs/Co_2P HMs was better than that of Ru NPs/Co_2P HMs implied the more interface between Ru and Co_2P with more electron transfer, which was confirmed by XPS in Figs. 2a–d and EXFAS spectra in Figs. 2e and f. It was worth noting that the Ru NPs/Co_2P HMs possessed the low Ru loading of 0.89 wt%, which was measured by ICP. After normalizing with Ru or Pt content, the mass catalytic activities of Ru NCs/Co_2P HMs, Ru NPs/Co_2P HMs and 20 wt% Pt/C at the overpotential of 200 mV were showed in Fig. S6 (Supporting information). The tendency in the HER performance standardized by content of Ru was found to be Ru NCs/Co_2P HMs (6.44 A/mg) > Ru NPs/Co_2P HMs (1.69 A/mg) > 20 wt% Pt/C (0.91 A/mg). In addition, Tafel plot was also confirmed the improvement of HER catalytic kinetics. As shown in Fig. 3b, the Ru NCs/Co_2P HMs possessed a smaller Tafel slope of 48 mV/dec than these of Ru NPs/Co_2P HMs (77 mV/dec), Co_2P HMs (97 mV/dec) and RuCo precursor (113 mV/dec), implying that the HER for the Ru NCs/Co_2P HMs followed a Volmer-Heyrovsky route as the rate determining step.

Electrochemical area represents the effective interface area between electrode and electrolyte. The electrochemical area (C_{dl}) of electrode was evaluated by cyclic voltammograms (Fig. S7 in Supporting information). As expected in Fig. 3c, the C_{dl} of the Ru NCs/Co_2P HMs (5.0 mF/cm^2) was higher than these of the Ru NPs/Co_2P HMs (2.1 mF/cm^2), Co_2P HMs (1.5 mF/cm^2) and RuCo precursor (0.5 mF/cm^2), indicating more HER catalytic sites of Ru NCs/Co_2P HMs. Electron-transfer kinetics were investigated by EIS measurement and the according Nyquist plots of these electrocatalysts were showed in Fig. 3d. The R_{ct} value of the Ru NCs/Co_2P HMs (45.8 Ω) was lower than those of the RuCo precursor (>1000 Ω), the Ru NPs/Co_2P HMs (62.6 Ω) and the Co_2P HMs (89.4 Ω) at an overpotential of 200 mV. Lower resistance stands for faster HER reaction rate, implying that the Ru NCs/Co_2P HMs was more active than the other samples. The endurance of electrocatalyst was a crucial factor for practical HER. As shown in Fig. 3e, at the respective overpotentials, after being operated continuously for 12 h, the current densities of 161 mA/cm^2 and 130 mA/cm^2 for Ru NCs/Co_2P HMs and commercial 20 wt% Pt/C were decreased to 155 mA/cm^2 (remain 96.3%) and 77 mA/cm^2 (remain 59%), respectively, implying the high catalytic stability of

Ru NCs/Co_2P HMs. Further, the HER polarization curves of Ru NCs/Co_2P HMs before and after *i-t* testing were achieved in Fig. 3f, and no visible change was detected. Additionally, as shown in Fig. S8 (Supporting information), XRD pattern and SEM image of Ru NCs/Co_2P HMs after *i-t* testing showed no obvious change of structure and morphology after long-term testing, implying the excellent structural robustness during the electrocatalytic HER process. In addition, the Ru NCs/Co_2P HMs also possessed the best activity among control Co_2P based sample for HER in 1.0 mol/L KOH solution, as showed in Figs. S9 and S10 (Supporting information). The superior electrochemical performance of HER both in acid and alkaline electrolyte may due to enhancive intrinsic catalytic activity by bonding between Ru and Co_2P in Ru NCs/Co_2P HMs, which were better than most previously reported electrocatalyst summarized in Table S1 (Supporting information).

The two half reactions of HER and OER for full water splitting were equally crucial for integrated efficiency [25–29]. Herein, for purpose of confirming the multifunction, the OER performance of Ru NCs/Co_2P HMs and other control samples were measured in 0.5 mol/L H_2SO_4 electrolyte. As shown in Fig. 4a, Ru NCs/Co_2P HMs possessed the high OER activity, which desired an overpotential of 197 mV to reach 10 mA/cm^2, lower than that of Ru NPs/Co_2P HMs (397 mV), RuCo precursor (699 mV), Co_2P (741 mV) and commercial RuO_2 (248 mV). The Tafel slope reflected the instinctive OER processes. As shown in Fig. 4b, the Tafel slope value of Ru NCs/Co_2P HMs was measured as 89 mV/dec which was smaller than those of Ru NPs/Co_2P HMs (109 mV/dec), Co_2P HMs (228 mV/dec) and RuCo precursor (224 mV/dec), implying that the reaction kinetics of the obtained Ru NCs/Co_2P HMs was faster than those of control samples. Electrochemical area was also analyzed by cyclic voltammograms to evaluate the C_{dl} of these samples, as shown in Fig. S11 (Supporting information) and Fig. 4c. The C_{dl} of the Ru NCs/Co_2P HMs (20.7 mF/cm^2) was higher than these of the Ru NPs/Co_2P HMs (16.2 mF/cm^2), Co_2P HMs (2.0 mF/cm^2) and RuCo precursor (1.5 mF/cm^2), implying more OER catalytic sites of Ru NCs/Co_2P HMs. Nyquist plots in Fig. 4d showed the R_{ct} value of Ru NCs/Co_2P HMs (54.4 Ω) was much smaller than those of RuCo precursor (>700 Ω), Ru NPs/Co_2P HMs (87.1 Ω) and Co_2P HMs (139.6 Ω) at the overpotential of 300 mV, implying a faster HER reaction rate of Ru NCs/Co_2P HMs. Given that as- prepared Ru NCs/Co_2P HMs was a multifunctional electrocatalyst toward both HER and OER in acidic electrolyte, a two-electrode electrolyzer applying Ru NCs/Co_2P HMs as both an anode and a cathode was assembled. For comparison, the benchmark noble metal-based electrolyzer of (−) 20 wt% Pt/C||RuO_2 (+) was constructed as well. As shown in Fig. 4e, this electrolyzer of (−) Ru NCs/Co_2P HMs||Ru NCs/Co_2P HMs (+) reached the current density of 10 mA/cm^2 at a voltage of 1.53 V in 0.5 mol/L H_2SO_4, which was superior to the benchmark of noble metal-based electrolyzer of (−) 20 wt% Pt/C||RuO_2 (+) (1.58 V). Further, the long-term electrochemical stability of the electrolytic cells was tested for 10 h. As shown in Fig. 4f, the current density of 12 mA/cm^2 was nearly unaltered for 10 h in 0.5 mol/L H_2SO_4 for the (−) Ru NCs/Co_2P HMs||Ru NCs/Co_2P HMs (+), which was steadier than that of the benchmark noble metal-based electrolyzer with an attenuation of 57%. The above results confirmed that the (−) Ru NCs/Co_2P HMs||Ru NCs/Co_2P HMs (+) couple possessed the high-efficiency water splitting performance and maintained perfect stability in the chronic electrolytic reaction, which exceeded those of the major reported metal-based bifunctional water-splitting catalysts in acid electrolyte summarized in Table S2 (Supporting information).

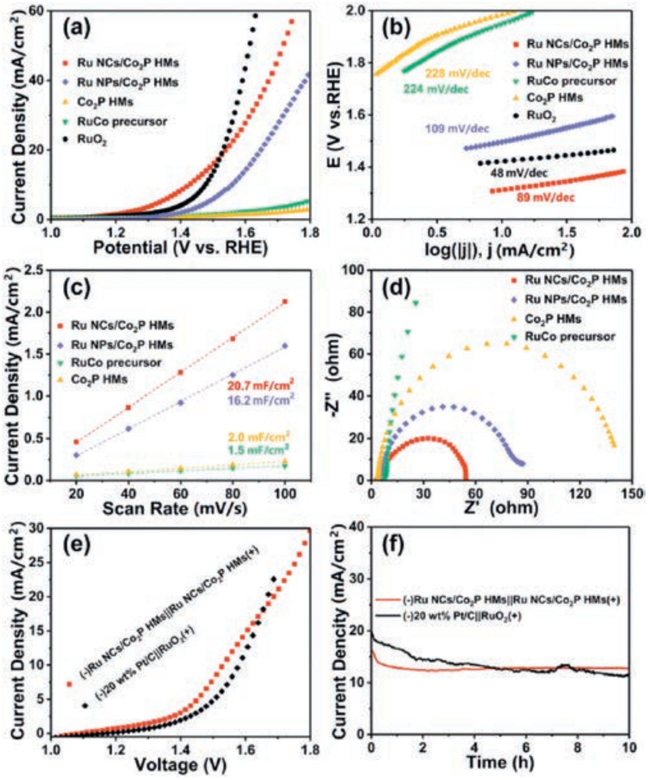

Fig. 4. (a) Polarization curves, (b) corresponding Tafel plots, (c) electrochemical area and (d) Nyquist plots at an overpotential of 300 mV of Ru NCs/Co_2P HMs, Ru NPs/Co_2P HMs, Co_2P HMs, RuCo precursor and RuO_2 for the OER in 0.5 mol/L H_2SO_4. (e) Polarization curves and (f) chronopotentiometry curves of the acidic electrolyzer using Ru NCs/Co_2P HMs as the cathode and anode (20 wt% Pt/C and RuO_2).

In summary, the ruthenium nanoclusters anchored on cobalt phosphide hollow microspheres (Ru NCs/Co_2P HMs) were synthesized *via* an *in situ* green phosphating approach without extrinsic phosphorus sources and the spatial limiting effect of RuCo precursor to restrict the agglomeration growth of Ru. The obtained Ru NCs/Co_2P HMs were wide-pH and multifunctional electrocatalyst for HER and OER. The Ru NCs/Co_2P HMs possessed efficient HER activity in acid electrolyte with an overpotential of 77 mV to drive 10 mA/cm^2 and good stability for 12 h, respectively. It was important that the Ru NCs/Co_2P HMs was also efficient for OER with an overpotential of 197 mV to drive 10 mA/cm^2. Based on the multifunction of Ru NCs/Co_2P HMs, the two-electrode system of (−) Ru NCs/Co_2P HMs||Ru NCs/Co_2P HMs (+) was assembled to drive full water splitting in acidic solution, and reached the current density of 10 mA/cm^2 at a voltage of 1.53 V, which was superior to that of the benchmark electrolyzer of (−) 20 wt% Pt/C||RuO_2 (+) (1.58 V). The comprehensive and excellent HER and OER catalytic activities of Ru NCs/Co_2P HMs were attributed to the merits of porous structure of Co_2P, uniform distribution of Ru nanoclusters and regulatory interface catalytic activity between Co_2P and Ru by electron transfer.

Declaration of competing interest

The authors declare that there are no conflicts of interest.

Acknowledgments

This work was supported by Fundamental Research Funds for Central Universities of SCUT (No. D2182400), Tip-top Scientific and Technical Innovative Youth Talents of Guangdong Special Support Program (No. 2016TQ03N541), Guangdong Natural Science Funds for Distinguished Young Scholar (No. 2017B030306001) and the National Natural Science Foundation of China (No. 51972147). We thank the photoemission endstations BL1W1B in Beijing

Synchrotron Radiation Facility (BSRF). Yunqie Deng thanks Jie Tang for selfless assistance and company.

Appendix A. Supplementary data

Supplementary material related to this article can be found, in the online version, at doi:https://doi.org/10.1016/j.cclet.2020.03.076.

References

[1] Y. Zheng, Y. Jiao, Y. Zhu, et al., Nat. Commun. 5 (2014) 1–8.
[2] Z. Xiao, Y. Wang, Y.C. Huang, et al., Energy Environ. Sci. 10 (2017) 2563–2569.
[3] Y. Deng, Z. Liu, A. Wang, et al., Nano Energy 62 (2019) 338–347.
[4] K. Xia, J. Guo, C. Xuan, et al., Chin. Chem. Lett. 30 (2019) 192–196.
[5] Y. Wang, Y. Yu, R. Jia, C. Zhang, B. Zhang, Nat. Sci. Rev. 6 (2019) 730–738.
[6] Y. Wang, W. Zhou, R. Jia, Y. Yu, B. Zhang, Angew. Chem. Int. Ed. 59 (2020) 5350–5354.
[7] J. Li, M. Yan, X. Zhou, et al., Adv. Funct. Mater. 26 (2016) 6785–6796.
[8] Y. Zeng, Y. Wang, G. Huang, et al., Chem. Commun. 54 (2018) 1465–1468.
[9] Y. Ji, J. Xie, Y. Yang, et al., Chin. Chem. Lett. 31 (2019) 855–858.
[10] R. Zhang, X. Wang, S. Yu, et al., Adv. Mater. 29 (2017) 1605502.
[11] E.J. Popczun, J.R. McKone, C.G. Read, et al., J. Am. Chem. Soc. 135 (2013) 9267–9270.
[12] R.B. Wexler, J.M.P. Martirez, A.M. Rappe, ACS Catal. 7 (2017) 7718–7725.
[13] G. Li, J. Wang, J. Yu, et al., Appl. Catal. B: Environ. 261 (2020) 118147.
[14] T. Liu, P. Li, N. Yao, et al., Angew. Chem. Int. Ed. 58 (2019) 4679–4684.
[15] X. Huang, X. Xu, C. Li, et al., Adv. Energy Mater. 9 (2019) 1803970.
[16] J. Yu, G. Li, H. Liu, et al., Adv. Funct. Mater. 29 (2019) 1901154.
[17] C. Wei, C. Cheng, B. Zhou, et al., Part. Part. Syst. Charact. 32 (2015) 831–839.
[18] B. Wang, H.B. Wu, L. Zhang, X.W. Lou, Angew. Chem. Int. Ed. 52 (2013) 4165–4168.
[19] J. Xu, T. Liu, J. Li, et al., Energy Environ. Sci. 11 (2018) 1819–1827.
[20] J. Chang, L. Feng, C. Liu, W. Xing, X. Hu, Angew. Chem. Int. Ed. 53 (2014) 122–126.
[21] J. Deng, H. Li, J. Xiao, et al., Energy Environ. Sci. 8 (2015) 1594–1601.
[22] J. Chang, L. Feng, C. Liu, W. Xing, X. Hu, Energy Environ. Sci. 7 (2014) 1628–1632.
[23] H. Chen, X. Ai, W. Liu, et al., Angew. Chem. Int. Ed. 58 (2019) 11409–11413.
[24] J. Mao, C.T. He, J. Pei, et al., Nat. Commun. 9 (2018) 1–8.
[25] K. Fan, H. Chen, Y. Ji, et al., Nat. Commun. 7 (2016) 1–9.
[26] F. Song, X. Hu, Nat. Commun. 5 (2014) 1–9.
[27] B. Zhang, X. Zheng, O. Voznyy, et al., Science 352 (2016) 333–337.
[28] L. Zeng, L. Yang, J. Lu, et al., Chin. Chem. Lett. 29 (2018) 1875–1878.
[29] J.J. Xu, C.H. Xiao, S.J. Ding, Chin. Chem. Lett. 28 (2017) 748–754.